Observational studies of short vertical wavelength gravity waves and interaction with QBO winds

R. A. Vincent[1], M. J. Alexander[2*]

[2]Northwest Research Associates, CoRA Office, 3380 Mitchell Lane, Boulder, CO 80301, USA

[1]Physics, School of Physical Sciences, University of Adelaide, Adelaide, SA 5005, Australia

Key Points:

- Combined superpressure balloon and radiosonde observations are used to study inertia-gravity waves at the equator
- Eastward and westward wave packets with 1 and 3 day periods are identified and momentum fluxes computed
- Contributions to the QBO are substantial for the short event periods considered.

[*]Northwest Research Associates. CoRA Office, 3380 Mitchell Lane, Boulder, CO 80301, USA

Corresponding author: M. Joan Alexander, `alexand@nwra.com`

Abstract

The quasi-biennial oscillation (QBO), a ubiquitous feature of the zonal mean zonal winds in the equatorial lower stratosphere, is forced by selective dissipation of atmospheric waves that range in periods from days to hours. However, QBO circulations in numerical models tend to be weak compared with observations, probably because of limited vertical resolution that cannot adequately resolve gravity waves and the height range over which they dissipate. Observations are required to help quantify wave effects. The passage of a superpressure balloon (SPB) near a radiosonde launch site in the equatorial Western Pacific during the transition from the eastward to westward phase of the QBO at 20 km permits a coordinated study of the intrinsic frequencies and vertical structures of two inertia-gravity wave packets with periods near 1-day and 3 days, respectively. Both waves have large horizontal wavelengths of about 970 and 5500 km. The complementary nature of the observations provided information on their momentum fluxes and the evolution of the waves in the vertical. The near 1-day westward propagating wave has a critical level near 20 km, while the eastward propagating 3-day wave is able to propagate through to heights near 30 km before dissipation. Estimates of the forcing provided by the momentum flux convergence, taking into account the duration and scale of the forcing, suggests zonal force of about 0.3-0.4 $\mathrm{ms^{-1}day^{-1}}$ for the 1-day wave and about 0.4-0.6 $\mathrm{ms^{-1}day^{-1}}$ for the 3-day wave, which acts for several days.

1 Introduction

Tropical gravity waves play a major role in driving tropical circulation above the tropopause. In particular, the tropical quasi-biennial oscillation (QBO) in zonal mean zonal winds of the lower stratosphere is primarily driven by dissipation of gravity waves, and a growing body of evidence shows the phase of the QBO to be important to climate prediction at sub-seasonal to interannual timescales (Boer & Hamilton, 2008; Scaife et al., 2014; Smith et al., 2016; Marshall et al., 2017; Garfinkel et al., 2018; Lim et al., 2019). As a result, there is an increasing effort to simulate a realistic QBO in global models, and this is currently achieved through parameterization of non-orographic gravity wave drag (Kawatani & Hamilton, 2013; Butchart et al., 2018). Unfortunately, the QBO tends to be a weaker source of predictability in the models than observations suggest it to be (M. J. Alexander & Holt, 2019), and limitations in fidelity of model representations of

the QBO may be responsible. This puts a special emphasis on better understanding of tropical gravity waves and their interactions with the QBO.

A major reason that modeled QBO circulations are weak in the lower stratosphere is because parameterized gravity wave drag tends to be weaker there than at upper levels near 10hPa. Weaknesses in gravity wave parameterization methods may be partly to blame. Evidence suggests that increasing model vertical resolution improves the simulation of the QBO (Giorgetta et al., 2002; Richter et al., 2014), because resolved tropical wave drag increases at higher vertical resolution (Holt et al., 2016). These resolved waves may include Kelvin waves, mixed Rossby-gravity waves, and inertia-gravity waves. If vertical resolution is too coarse, these resolved large-scale waves will dissipate at altitudes well below their critical levels, which could lead to consistently weaker forces on the mean flow in models than in the real atmosphere. Precisely how closely waves of all horizontal scales approach their critical levels before dissipating is therefore a significant source of uncertainty in modeling the QBO.

As waves propagate vertically and approach their critical levels in QBO shear, their phase speeds c_0 approach the wind speed $U(z)$. The Kelvin and gravity wave dispersion relation, for example,

$$m = Nk_h/(U - c_o), \tag{1}$$

tells us that the vertical wavelength $\lambda_z = 2\pi/|m|$ shrinks in proportion to the intrinsic phase speed $|U-c_0|$. Here, N is the Brunt-Vaisala frequency, and k_h is the horizontal wavenumber. While dispersion relations differ in detail for other tropical waves, λ_z still shrinks as the waves approach critical levels, and without very high vertical resolution, model diffusion may eliminate a wave far below its critical level. This is important to the force imparted to the mean flow when the wave dissipates because momentum flux F_M is constant for waves propagating without dissipation, while the drag force D occurs with dissipation of F_M given by,

$$D = -\frac{1}{\rho}\frac{dF_M}{dz}. \tag{2}$$

If, due to coarse vertical resolution, the wave dissipates several km lower (say at $\rho(z_1)$) than it should (say at $\rho(z_2)$), the resulting force may be 50% smaller ($\rho(z_1)/\rho(z_2)$) due to the exponential decrease in density with altitude.

Fine vertically-resolved observations with global coverage are rare. Satellite measurements with the highest vertical resolution have shown tropical waves with vertical

wavelengths as short as ~4 km, which is close to the vertical resolution limit (M. J. Alexander & Ortland, 2010; Wright et al., 2011), but the zonal resolution of these data limits the observable zonal wavelengths to at best 5000 km (S. P. Alexander et al., 2008). Although not made on a global scale, high-resolution radiosonde soundings do have a vertical resolution of $O \sim 50$ m, and such soundings have been used to study wave parameters such as vertical and horizontal wavelength, kinetic and potential energy, as well as to investigate wave sources (Tsuda et al., 1994; Allen & Vincent, 1995; Vincent & Alexander, 2000; Lane et al., 2003; Wang & Geller, 2003; Wang et al., 2005; Geller & Gong, 2010; Gong & Geller, 2010; Murphy et al., 2014).

A disadvantage of satellite and radiosonde GW observations is that the wave parameters are made in a ground-based reference frame so it is the ground-based frequency ω that is inferred. However, it is the wave frequency relative to the background wind, the intrinsic frequency $\hat{\omega}$, that determines important wave parameters (Fritts & Alexander, 2003). This limitation can be overcome by using superpressure balloon (SPB) observations. SPB float on an a constant density surface with typical altitudes in the range 16 to 20 km, depending on the balloon diameter, moving with the mean wind. In recent years, superpressure balloon (SPB) measurements have been used to infer gravity and planetary wave parameters at latitudes ranging from the Arctic to the Antarctic (Vial et al., 2001; Hertzog et al., 2002; Vincent et al., 2007; Boccara et al., 2008; Hertzog et al., 2008, 2012; Podglajen et al., 2016), but to date only a few circumnavigating tropical trajectories have been analyzed (Jewtoukoff et al., 2013). The limitation of these measurements has been the lack of vertical structure information, which must be indirectly inferred (Boccara et al., 2008; Vincent & Hertzog, 2014).

High-resolution radiosondes provide complementary information to SPB, a factor which we exploit to study low-frequency tropical gravity waves at locations where balloon trajectories pass near a high-resolution radiosonde launch site. The SPB measurements provide detailed information on gravity waves as a function of intrinsic frequency, but without other meteorological data it can be difficult to put the GW measurements in context. In contrast, radiosondes provide vertical snapshots of the atmosphere, typically from the surface to a 25 to 30 km height range between the launch and burst heights. By combining SPB and radiosonde observations it is possible to overcome the limitations of each technique.

The advantages of combining near simultaneous observations made in both space and time are demonstrated by using observations made by an SPB and by high-resolution radiosondes in the western Pacific. This study arises from SPB measurements made in the PreConcordiasi campaign that took place in the equatorial regions in 2010 (Podglajen et al., 2014, 2016). Three SPB were launched from the Seychelles in this campaign. In particular, one balloon (SPB2) approached close to Manus Island in the Western Pacific, from which radiosondes were launched from Momote Airfield (2.05°S, 147.43°E) on a twice daily basis. We report on a case study of GW parameters determined using combined SPB and radiosonde data at a time when the closest approach of the SPB to Momote occurred. At this time the QBO was transitioning from its eastward to its westward phase in the lower stratosphere. We find two large-scale ($\sim$970 and 5500 km) gravity wave packets with short vertical wavelengths and one these wave packets, in particular, is inferred to be approaching a critical level within 1 km of the observation height.

The paper is organised as follows. In section 2, the SPB and radiosonde observations are introduced. During the period when the SPB is closest to Momote two specific GW packets are identified and analyzed in section 3, including analyses of the GW changes with altitude appearing in the radiosonde records. Finally, in section 4 we make an estimate of the mean-flow forcing effects of these waves, and discuss the implications for future analyses of tropical superpressure balloon measurements currently underway through the Strateole-2 project.

2 Observations

2.1 Superpressure Balloon Observations

Superpressure balloons (SPB) are closed, inextensible, spherical envelopes filled with a fixed amount of gas. SPB ascend after launch until they reach a level where the balloon density matches the atmospheric density and then float on this isopycnic surface under the influence of the horizontal winds, acting as a quasi-Lagrangian tracer. Using GPS measurements of horizontal and vertical position with a time resolution of minutes means that the full GW spectrum can be observed. During the PreConcordiasi campaign, three 12-m diameter SPB were deployed by the Centre National d'Etudes Spatial (CNES) from the Seychelles between February and May 2010. Each balloon drifted on a constant density surface ($\rho_o \sim 0.1$ kgm^{-3}), with two SPB circumnavigating the globe within a
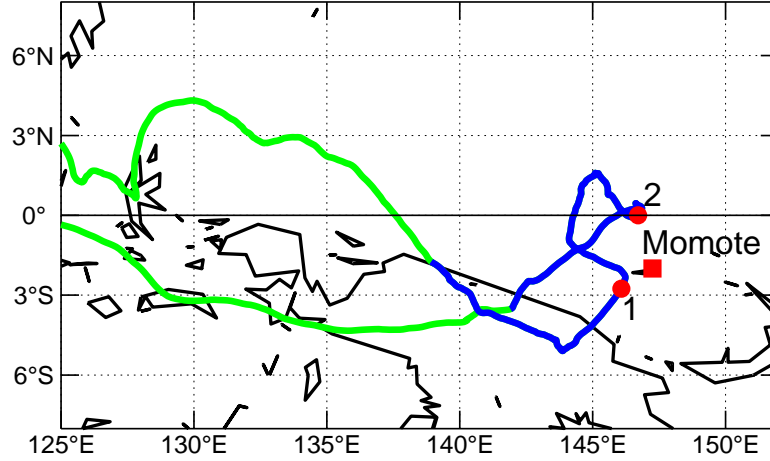
Figure 1. The green/blue line is the trajectory of SPB2 during the PreConcordiasi campaign in the period 9 April to 8 May 2010 (day of year (DoY) 99 to 128). The blue section shows the path from -2 to +4 days around the time of closest approach (DoY 117.5∼12 UT on 27 April) to Momote (red square). The red circles labelled 1 and 2 denote the central locations of two wave packets (see Section 3.1 for details).

±15° band around the equator. The trajectories are shown in Podglajen et al. (2014). The balloons carried GPS receivers to log their position and sensors to measure pressure and temperature with an overall time resolution of 1 min (see Vincent and Hertzog (2014) for details of the instruments and their accuracy).

Here we focus on the flight of SPB2, which flew at a mean altitude of 19.4±0.1 km between 19 February and 8 May 2010. In the early part of April it moved eastward under the influence of the prevailing winds, but about 15 April the winds at the float level made a transition to westward flow as the winds associated with the quasi-biennial oscillation (QBO) descended from the middle stratosphere. Figure 1 shows the trajectory in the period from 9 April to 8 May 2010, with the blue section highlighting the trajectory in the 6-day period when the balloon was closest to Momote.

2.2 Radiosonde Observations

Radiosondes were launched twice daily (00 and 12 UT) from Momote Airfield on Manus Island (Long, 2015). Using Vaisala RS80-15GH radiosondes, pressure, temperature, dew point, wind direction and speed data were acquired every 10 s, which approx-
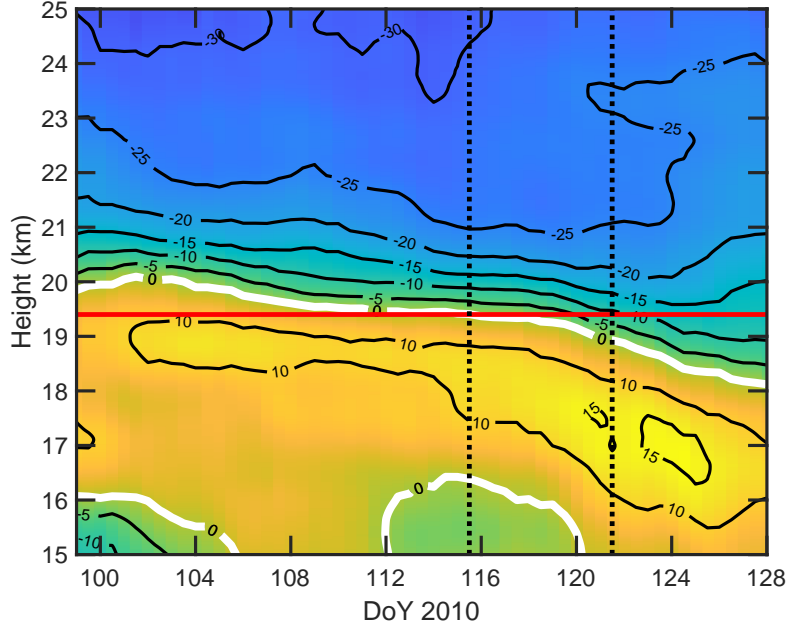
Figure 2. Cross-section of zonal winds as a function of height and day of year (DoY) constructed from radiosonde observations made at Momote. The red line shows the mean height of SPB2 (19.4 km), while the dotted lines indicate the 6-day interval centered around the date of closest approach of SPB2 to Momote (DoY 117.5).

¹⁵³ imated to height intervals that varied from less than 10 m to about 50 m depending on ¹⁵⁴ the balloon ascent rate. For the purposes of this work the data were spline interpolated ¹⁵⁵ onto a uniform 30 m height grid. The upper levels attained varied, but usually exceeded ¹⁵⁶ 25 km. To ensure a uniform dataset, the upper limit here was restricted to 25 km. Mean ¹⁵⁷ zonal winds ($\overline{u}$) as a function of time and height are shown in Figure 2. Short term variations are reduced by using 7-day sliding averages of $\overline{u}$. It is apparent that during the interval shown in Fig. 2 that the stratospheric winds at the SPB float level changed systematically from about 5 ms^{-1} eastward to 12 ms^{-1} westward as the westward phase of the QBO descended. Meridional winds were variable and weak and are not shown. For reference, the average northward speed between locations 1 and 2 shown in Fig. 1 was about 2-3 ms^{-1}.

¹⁶⁴ Ambient factors that influence GW propagation in the vertical during the interval from day of year (DoY) 115.5 to 121.5 (25 April to 1 May 2010) are shown in Figure 3. The mean zonal wind profile is displayed in Fig 3a, while Figs 3b,c show the mean temperature and the square of the Brunt-Vaisala (BV) frequency, N^2, respectively. The
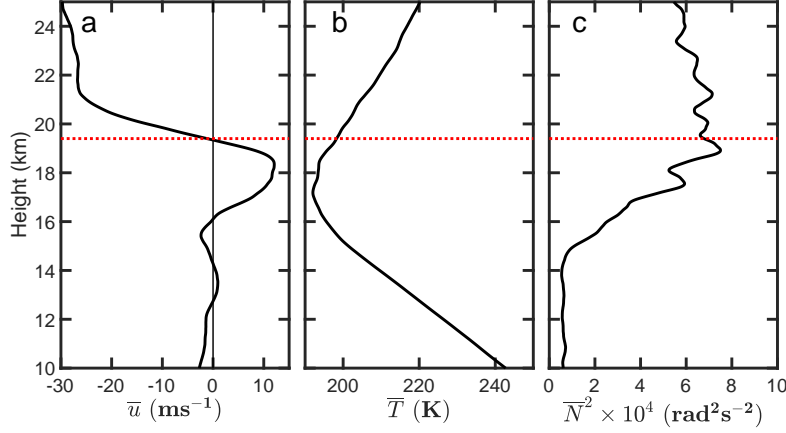
Figure 3. Vertical profiles of (a) zonal wind ($\overline{u}$), (b) temperature ($\overline{T}$) and (c) $\overline{N}^2$. Each profile is an average from radiosonde flights between DoY 115.5 and 121.5. In order to emphasize the mean structure, the $\overline{N}^2$ profile has been smoothed by a 1-km wide running mean. The red dashed lines indicate the mean flight altitude of SPB2.

latter is defined as

$$N^2 = \frac{g}{\overline{T}}\left(\frac{g}{c_p} + \frac{d\overline{T}}{dz}\right) \tag{3}$$

where g is the acceleration due to gravity, $\overline{T}$ and $d\overline{T}/dz$ are mean temperature and its vertical gradient and c_p is the specific heat at constant pressure. At the float altitude $N^2 \sim 7.23\,10^{-4}$ s^{-2}, (i.e a BV period of ~ 234 sec). This parameter is also important in determining the balloon response to GW (Vincent & Hertzog, 2014) and in the GW dispersion relation (Fritts & Alexander, 2003)

$$m^2 = \frac{N^2 - \hat{\omega}^2}{\hat{\omega}^2 - f^2}k_h^2 - \frac{1}{4H^2}, \tag{4}$$

where m and k_h are the vertical and horizontal wavenumbers, f is the inertial frequency and H is the density scale height. At Momote, $f \sim 5.1 \times 10^{-6}$s^{-1} ($\tau_f \sim 14$ day).

3 Gravity Wave Case Studies

3.1 SPB Observations

To study GW, the SPB data were high-pass filtered with a 10-day cut-off to remove mean wind effects. Prior to analysis the raw float height data were checked for sudden decreases from the notional 19.4 km float altitude caused by passage across high, cold, clouds which cause changes in the internal balloon temperature and pressure. These height

decreases are of short duration (less than a few hour at most), but also affect the pressure, temperature and zonal wind measurements because of the vertical gradients in these quantities. The relevant data were interpolated over where these events were identified and do not materially affect our studies since we are focused on waves with periods longer than about 1 day.

Previous SPB studies show that GW effects are packet-like (Vincent et al., 2007; Boccara et al., 2008; Hertzog et al., 2008). Hence, the SPB data were analyzed using S-transforms, which decomposes the data in time-frequency space (Stockwell et al., 1996), akin to the Morlet wavelet methodology used in the studies cited above. The S-transform spectrum of the GW total energy KE + PE,

$$E_T = \frac{1}{2}\left(u'^2 + v'^2\right) + \frac{1}{2}\left(\frac{g^2}{N^2}\frac{T'^2}{\overline{T}^2}\right), \tag{5}$$

is shown in Figure 4. T' is the GW-induced temperature perturbation, derived after removing the effect of SPB vertical displacements in the presence of the background temperature gradient (Vincent & Hertzog, 2014).

Since we are concerned with waves close to the equator (Fig. 1), where f is small, we can use the so-called mid-frequency approximation, that is GW with intrinsic frequencies in the range $N^2 >> \hat{\omega}^2 >> f^2$. A particular emphasis is on wave periods longer than 1 day, so only wave periods between 5 days and 16 hr (frequencies between 0.2 and 1.5 cyc d^{-1}) are shown in Fig 4. This analysis revealed that there are two distinct features in the 6-day interval of interest. These spectral features, 1 and 2, are highlighted by the white boxes in Figure 4. Similar peaks at the same frequencies and times also appear in spectra of other measured parameters, such as pressure, albeit with somewhat different relative amplitudes. We conclude that these features are associated with long-period gravity waves.

To quantify the basic parameters of the regions or 'packets' evident in Fig. 4, Gaussian functions were fit in time-frequency space. The results are summarized in Table 1. 'Packet' 1 is of short duration, with a width $(2 \times \Delta t_o)$ of about 1.6 days and an associated wide spread in frequency (0.40 d^{-1}). The corresponding values for 'packet' 2 are $\sim$5 days and 0.14 d^{-1}, respectively. The intrinsic periods for 1 and 2 are 0.95 (0.87-1.33) days, and 2.77 (2.33-3.44) days, where the values in brackets denote the 95% uncertainties derived from the uncertainties in the Gaussian fitting parameters.
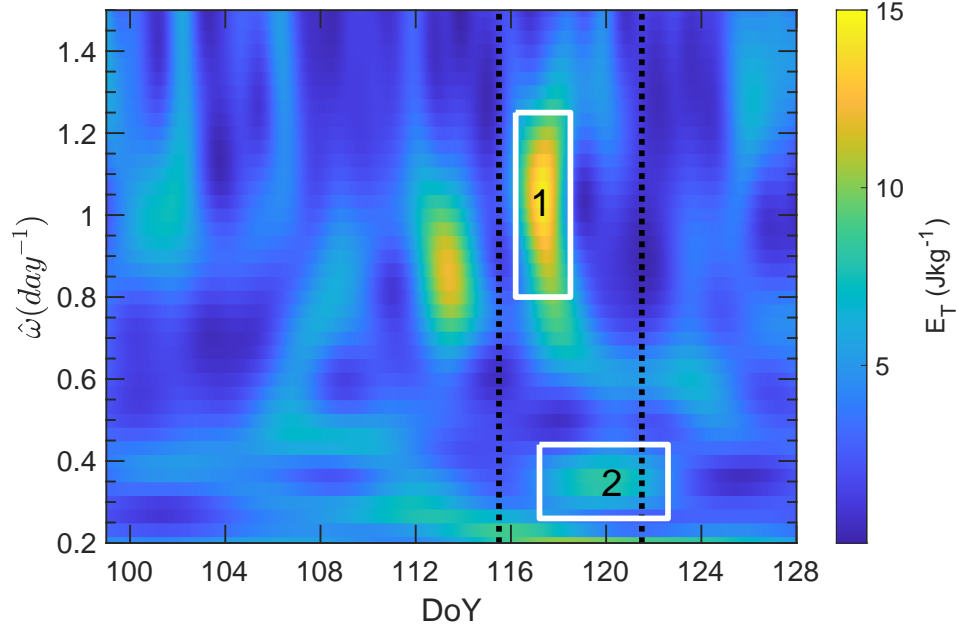
Figure 4. Time-frequency S-transform spectrum of the total energy (E_T=KE+PE) from SPB observations from DoY 99 to 128, 2010. The white boxes labelled 1 and 2 denote spectral regions that are subject to further analysis. The vertical dashed lines indicate the 6-day interval corresponding to the interval centered around the date of closest approach to Momote. Note that units for $\hat{\omega}$ here are cyc d^{-1}, but elsewhere rad d^{-1} unless otherwise noted.

Table 1. Basic parameters associated with wave packets 1 and 2 (Fig. 4). E_{max} is the peak total energy of each packet. t_o and $\hat{\omega}$ are the respective dates and frequencies of the peak values and Δt_o and $\Delta\hat{\omega}$ are the associated *rms* widths of the spectral features. Lat. and Lon. give the latitude and longitude of the SPB position at the times of peak amplitude.

Parameter	1	2
E_{max} (Jkg^{-1})	15.1	8.23
t_o (DoY)	117.3	119.8
Δt_o (day)	0.79	2.47
$\hat{\omega}$ (cyc d^{-1})	1.05	0.36
$\Delta\hat{\omega}$ (cyc d^{-1})	0.20	0.07
Lat. (deg)	-2.76	0.00
Lon. (deg)	146.08	146.71

215   With respect to packet 1, which has a period close to one day, it should be noted

216   that there is a diurnal deviation from isopycnic behavior associated with expansion of

217   the balloon envelope due to solar heating (Podglajen et al., 2016). However, the verti-

218   cal displacements associated with this event are many times the amplitude of the solar

219   heating effect and the phase of the oscillation is in anti-phase/quadrature with that ex-

220   pected for the sunrise/sunset cycle. We conclude that the solar heating effect is not rel-

221   evant in this particular case.

222   It is now straightforward to obtain the relevant wave parameters following the anal-

223   ysis outlined in section 5 of Vincent and Hertzog (2014), with some modifications. Briefly,

224   for each packet the perturbation wind field was rotated through an angle θ required to

225   maximize the value of $U_{||}$, the modulus of the horizontal wind perturbation. This gives

226   the horizontal direction of travel with an ambiguity of $\pm 180°$. The intrinsic phase speed

227   $\hat{c}$ can be derived from the real part of the cross-spectrum between the pressure pertur-

228   bation, p', and $U_{||}$. However, instead of computing wave momentum fluxes by the method

229   described in Vincent and Hertzog (2014) we use a more direct estimate. In general, the

230   SPB response to an isopycnic surface disturbed by a gravity wave will not be in-phase

231   with the wave (Nastrom, 1980; Vincent & Hertzog, 2014), but at intrinsic frequencies

232   much less than N, the phase shift is negligible and the balloon follows the isopycnal sur-

233   face. In this limit, the vertical wave displacement ζ' can be derived directly using

$$\zeta' = \frac{\zeta_b}{|Z_{EDS}|} \tag{6}$$

235   where ζ_b is the vertical displacement of the balloon from its equilibrium density surface

236   (EDS). Z_{EDS} is a factor that depends on the prevailing meteorological conditions. In

237   the low-frequency limit here

$$|Z_{EDS}| = \frac{2N^2}{3\omega_B^2} = \frac{\left(\frac{d\overline{T}}{dz} + \frac{g}{c_p}\right)}{\left(\frac{d\overline{T}}{dz} + \frac{g}{R_a}\right)}. \tag{7}$$

239   R_a is the atmospheric gas constant. Using the temperature profile shown in Fig 3b with

240   $d\overline{T}/dz = 4.8$ K/km at the SPB float altitude, gives $|Z_{EDS}| = 0.37$ or $\zeta' = 2.68\,\zeta_b$. Hence,

241   the GW vertical velocity perturbation is $w' = \partial\zeta'/\partial t$. Computing the zonal and merid-

242   ional fluxes $\overline{u'w'}$ and $\overline{v'w'}$ then resolves the θ ambiguity in the horizontal propagation

243   direction. The horizontal wavenumber is give by $k_h = \hat{\omega}/\hat{c}$, with components (k, l), and

244   the vertical wavenumber is derived from equation (4). The ground-based frequency ω

245   and period τ_o are then found via the Doppler shift equation, $2\pi/\tau_o = \omega = \hat{\omega} + k\bar{u}\cos\theta +$

246    $l\bar{v}\sin\theta$ where $\bar{u}$ and $\bar{v}$ are the mean wind components at the float altitude (Vincent &

247   Hertzog, 2014). The ground-based phase speed, c_o, and its direction θ_o, are derived as

248   described by Boccara et al. (2008). Table 2 summarizes the results.

Table 2.   Gravity wave parameters derived from SPB observations. u'_{rms} is the computed horizontal perturbation amplitude. $\hat{c}$ (c_o) and θ (θ_o) are the intrinsic (ground-based) phase speed and azimuth of propagation (anticlockwise from east). λ_h and λ_z are the respective horizontal and vertical wavelengths, and τ_o the ground-based period.

Parameter	1	2
u'_{rms} (ms^{-1})	3.2	2.2
$\rho_o \overline{u'_{\parallel} w'}$ (mPa)	4.3	0.7
$\hat{c}$ (ms^{-1})	11.4	22.1
θ (deg)	203	341
λ_h (km)	972	5375
λ_z (km)	2.7	5.2
τ_o (day)	1.75	3.14
c_o (ms^{-1})	6.4	19.8
θ_o (deg)	203	341

249   With these basic wave parameters it is now possible to examine the vertical and

250   horizontal propagation of the wave packets using gravity wave ray tracing techniques.

251   The basic, 7-day average, atmospheric profiles used are shown in Fig. 3. The method-

252   ology follows Marks and Eckermann (1995), which allows both the ray path and the wave

253   action, and hence wave amplitude, to be derived as a function of latitude, longitude, height

254   and time. Figure 5 shows the horizontal paths (Fig. 5c) of the two wave packets ema-

255   nating from their respective locations, together with plots of the vertical profile of their

256   respective intrinsic phase speeds and vertical wavelengths (Figs. 5a,b).

257   It is evident from Fig 5 that both $\hat{c}$ and λ_z become small for packet 2 at heights

258   between 17 and 18 km. This may indicate the source height for this wave is in the vicin-

259   ity of the tropical tropopause because a wave propagating from below would not likely

260   penetrate this layer without breaking. In contrast, packet 1 has non-negligible phase speeds

261   and wavelengths at heights below the SPB level, but these values rapidly decrease above
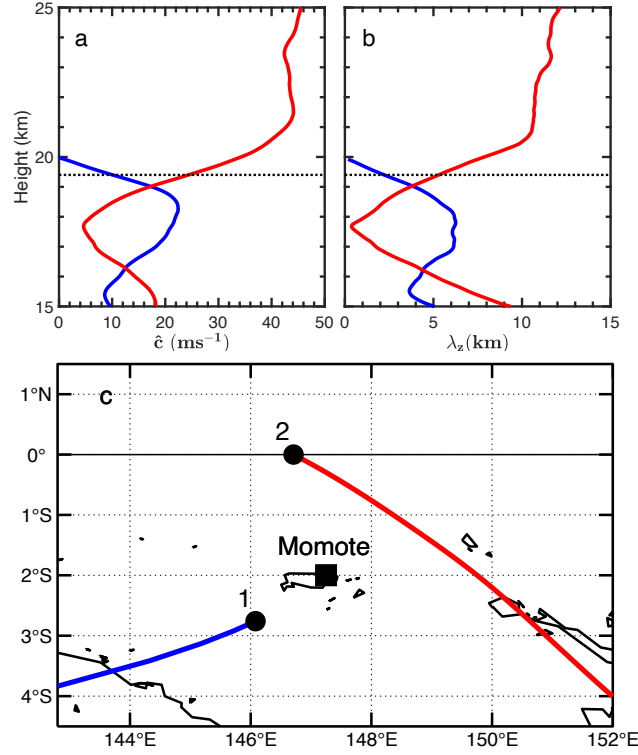
Figure 5. (a) Vertical profiles of GW intrinsic phase speed, $\hat{c}$, for packets 1 (blue) and 2 (red). (b) Profiles of vertical wavelengths, λ_z. (c) Horizontal projection of ray paths for heights above the balloon float altitude. In (a) and (b) the dotted line shows the mean float altitude of the SPB.

the float altitude. Near 20 km the wave encounters a critical level where the phase speed matches the background wind. A critical level so close to the balloon level calls into question the accuracy of the inferred wave parameters as $\hat{\omega} \rightarrow f$ (Fritts & Alexander, 2003). The ray path was terminated after a few hours, when the vertical wavelength had decreased to less than 0.5 km.

Two height regimes are appropriate when considering Momote radiosonde and SPB GW comparisons. Reverse ray tracing for packet 1 (not shown) suggests that it passed close to Momote a few hours ahead of the time it was observed by the SPB *i.e.* about 00 UT on day 117. It also appeared to emanate from somewhere in the altitude region above 15 km. The wave amplitude at the time of closest approach to Momote is computed to be $\sim$2.75 ms^{-1}. Conversely, the ray for packet 2 passes within about 160 km of Momote some 2-3 hr after launch *i.e.* closest approach at $\sim$21 UT on day 119 (April

274 29). At this time, the altitude of the packet is near 20 km and the computed horizon-

275 tal perturbation amplitude is about 2.5 ms^{-1}. Sensitivity tests show that varying the

276 launch azimuth, θ_o, by $\pm 5°$ meant the ray paths passed within either 190 km or 150 km

277 of Momote. Changing the ground-based phase speed by $\pm$ 10% did not make a signif-

278 icant difference to the distance of closest approach, but did change the time of closest

279 approach by about $\pm$ 1 hr.

280 These results indicate that packet 1 influences the radiosonde observations at heights

281 between 15 and 20 km near day 117, while the effects of packet 2 will be felt at heights

282 at and above 20 km, particularly near day 120. However, packet 2 in particular has a

283 large horizontal scale and may be present across the region covered by the radiosonde

284 site and the balloon path for many days and also at significant depths below the SPB

285 float altitude.

286 ### 3.2 Momote Radiosonde GW Observations

287 As a radiosonde ascends it acts as a passive tracer of GW motions, giving a ver-

288 tical 'snapshot' of the wavefield, provided the ascent rate is greater than a few ms^{-1} and

289 the background winds are less than 10 times the ascent rate (Gardner & Gardner, 1993).

290 The background state is often determined and removed by fitting low-order polynomi-

291 als to tropospheric or stratospheric wind and temperature profiles (Allen & Vincent, 1995;

292 Wang & Geller, 2003). Our focus is on the region around the tropopause and lower strato-

293 sphere where there is a large shear in $\overline{u}$, and polynomial fits lead to large discontinuities

294 at the boundaries of the residual profiles. Accordingly, a somewhat different approach

295 is used for background removal. Seven-day running means of the wind and temperature

296 components are subtracted from the individual profiles to get the GW-induced pertur-

297 bations. This method is akin to the technique used by Kim and Alexander (2015) who

298 studied tropical wave temperature perturbations as a function of height derived from West-

299 ern Pacific radiosonde observations.

300 The leftmost panels in Figure 6 show residual profiles for a thirteen-day period cen-

301 tered on day 120. Wavelike perturbations are evident in all profiles, showing downward

302 phase progression, indicative of upward energy propagation. These features are brought

303 out in a different way in image plots of the wind and temperature perturbations (Right:

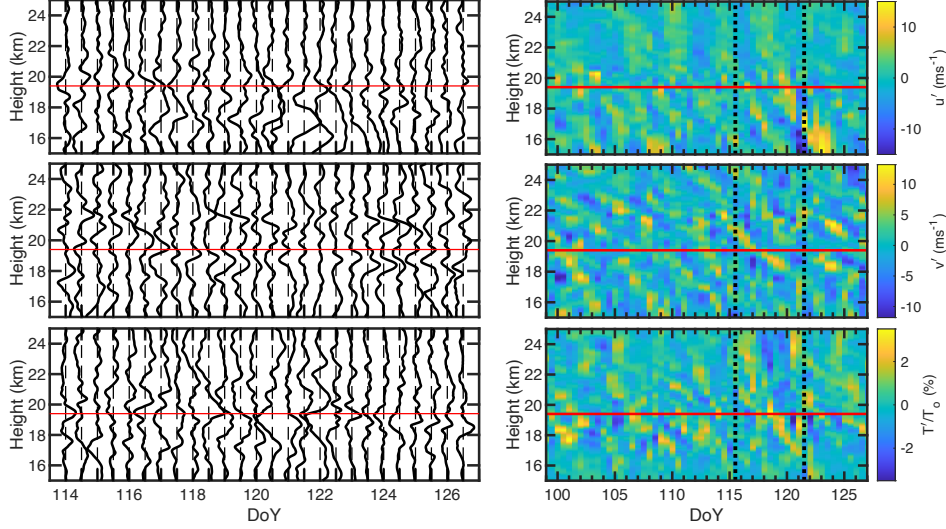304 Figure 6). The height-time phase tilts suggest dominant motions with ground-based pe-

Figure 6. Left Panels: Profiles of u' (top), v' (middle) and T'/T_o (bottom) for individual radiosonde soundings made at Momote between days 114 and 127 (see text for details). The spacing between profiles is equivalent to 15 ms^{-1} for the wind components and 3.75% for the fractional temperature perturbations. Right Panels: Image plots for u' (top), v' (middle) and T'/T_o (bottom) for days 99 to 127. The vertical lines indicate the period of closest approach to Momote and the red lines in both panels show the mean altitude of the SPB.

.

305 riods of a few days and increasing vertical wavelengths with increasing height. It should

306 be remembered that the 12-hr sampling rate means a 24-hr Nyquist period, so waves with

307 periods less than 24 hr will be difficult to see in the time series, but longer period waves

308 should be clearly visible. Hence, the wave field will be dominated by waves with peri-

309 ods of a day or longer.

310 **3.3 Stokes Parameters**

311 Gravity wave motions are elliptically polarized as a function of height. The Stokes-

312 parameters method is a way to analyse wave observations made using a variety of sound-

313 ing techniques in order to quantify the amplitudes and polarization (Vincent & Fritts,

314 1987; Eckermann & Vincent, 1989; Vincent et al., 1997; Vincent & Alexander, 2000; Schöch

315 et al., 2004). Eckermann (1996) provides an extensive analysis of the technique as ap-

316 plied to hodographs of wind perturbations (u', v') composed of a partially polarized wave

317 field that contains a coherent wave with peak amplitude $U_o = (u_o, v_o)$ plus unpolar-

ized isotropic fluctuations with variance $\overline{u_{noise}^2} + \overline{v_{noise}^2}$. Following Eckermann (1996), the parameters are defined as

$$I = \frac{1}{2}(\overline{u_o^2} + \overline{v_o^2}) + \overline{u_{noise}^2} + \overline{v_{noise}^2} = (\overline{u'^2} + \overline{v'^2}) \tag{8}$$

$$D = \frac{1}{2}(\overline{u_o^2} - \overline{v_o^2}) = \overline{u'^2} - \overline{v'^2} \tag{9}$$

$$P = \overline{u_o v_o \cos \delta} = 2\overline{u'v'} \tag{10}$$

$$Q = \overline{u_o v_o \sin \delta} \tag{11}$$

where the overbars denote time/height averaging of the perturbations. I is a measure of the kinetic energy associated with the wave field, while the other parameters can be used to determine factors of the polarization ellipse, such as the axial ratio AR which is the ratio of the major to minor axis and is related to the ratio of $\hat{\omega}$ to f (Eckermann & Vincent, 1989). The degree of polarization, dp, which quantifies the fractional contribution of any coherent wave motion to the total velocity variance is defined as

$$dp = \frac{(D^2 + P^2 + Q^2)^{1/2}}{I}, \tag{12}$$

Following Eckermann and Vincent (1989) we compute the Stokes parameters in vertical wavenumber space.

Since it is not possible to derive a unique direction of horizontal propagation from the Stokes analysis, this parameter was deduced by computing covariances between the wind and temperature perturbations. The direction is given by

$$\alpha = \tan^{-1}(\overline{v'\hat{T}}_{+90}, \overline{u'\hat{T}}_{+90}) \tag{13}$$

where the overbars indicate averages in height and $\hat{T}_{+90}$ is the Hilbert-transform of the temperature perturbations normalized by the background temperature (Vincent et al., 1997).

3.3.1 Packet 1

Three factors need to be considered. Firstly, packet 1 has short duration ($\sim$1 day), secondly, reverse ray tracing indicates that its closest approach to Momote occurs near 00UT on day 117 and thirdly, Figure 5 shows that only the 15-20 km height range need be considered. To accommodate the short duration, Stokes parameters were computed using just 3 radiosonde flights (days 116.5, 117.0 and 117.5). Results are summarized in Table 3, which shows the mean values ($\overline{X}$) for four parameters that encapsulate the whole

Table 3.   Summary of Stokes parameters for packet 1 computed from three radiosonde flights centered on day 117 and covering the height range 15-20 km. $\overline{X}$ is the mean value of each parameter and $\overline{\Delta X}$ is the associated mean absolute deviation (see text).

Parameter	$\overline{X}$	$\overline{\Delta X}$
I (m^{2}s^{-2})	35	11
dp	0.59	0.02
$|AR|$	7.0	3.7
α (deg)	249	42

analysis. The mean absolute deviation ($\Delta X = \Sigma(|X_i - \overline{X}|)/3$) is used to estimate the variability in the mean value.

The values of I and dp together indicate that the coherent wave has an amplitude $U_{rms} \sim 4.5$ ms^{-1}. D has a value ~ 5 m^{2}s^{-2}, so u_o and v_o are estimated to be about 5 and 4 ms^{-1}, respectively. The relatively large value of $|AR|$ implies near linear polarization. The horizontal direction of propagation α has quite a large deviation, but is consistent with overall propagation toward the south-west. This is in accord with the value of about 200° derived from the SPB observations (Table 2) and the ray tracing results (Fig 5).

3.3.2   Packet 2

The vertical extent of packet 2 is unknown, but given its large horizontal wavelength and long duration it is assumed that the packet will have a considerable depth. A height range of 18 to 25 km was chosen to study its characteristics since N^2 is constant over this height range (Fig. 3), although the background wind shows a strong westward shear. The results from the Stokes analysis are summarized in Figure 7. To focus on the longer term (several day) features, short term, intra-diurnal, variations in basic parameters (I, D, P and Q) were reduced using a (1/4, 1/2, 1/4) filter in time.

Packet 2 approaches closest to Momote during the interval day 118 to 122. Figure 7 shows that the mean value and standard error for the total variance is $I \sim 26\pm 1$ m^{2}s^{-2}, for $dp \sim 0.32 \pm 0.06$, $|AR| \sim 15 \pm 6$ and for the direction of propagation is
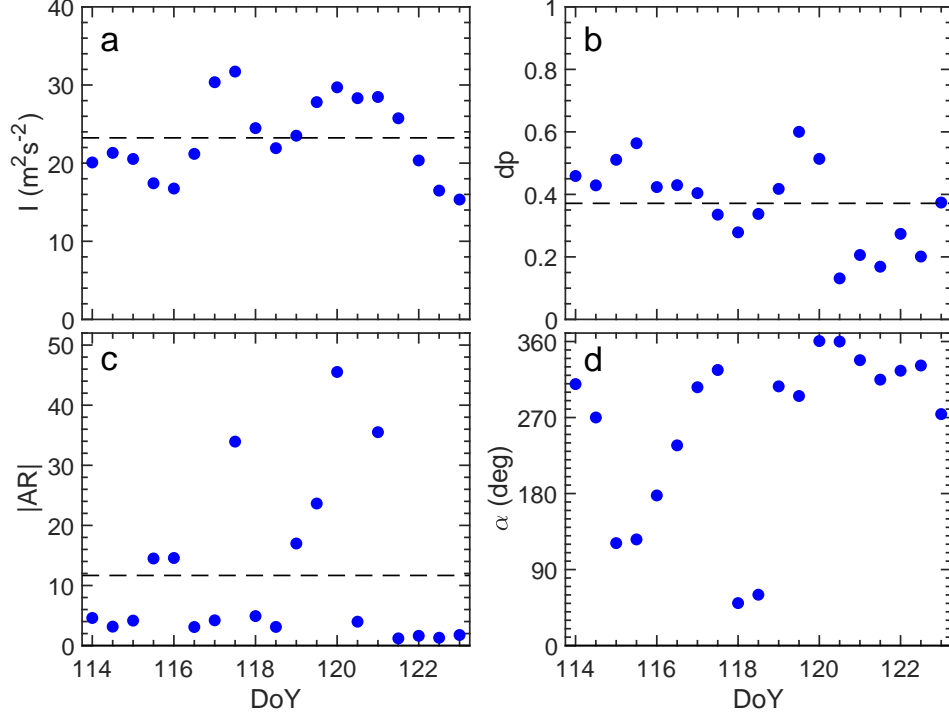
Figure 7. Values of (a) the total wind variance, I, (b) degree of polarization, dp, (c) modulus of the axial ratio, $|AR|$ and (d) horizontal direction of travel, α, derived using Stokes analyses of the radiosonde data taken every 12 hours over the 18-25 km height range at Momote. The dashed lines show the relevant mean values from days 114 to 123.

$\alpha \sim 348° \pm 15°$, anticlockwise from east *i.e.* propagation to the southeast. The large value of $\overline{|AR|}$ implies near linearity of the wave motions ($\hat{\omega} >> f$) and the combination of I and dp suggests that the coherent wave component has an *rms* amplitude of $U \sim 3$ ms^{-1}. Comparison with the amplitude and direction of wave motion estimated from the SPB observations (Table 2, column 2) shows good agreement with the values derived from the radiosonde observations. Finally, It should be noted that recalculating the Stokes parameters over different height ranges, such as 16-23 km, do not change the results significantly, which is likely due to the fact that the Stokes results will be most sensitive to altitudes $\sim 18 - 20$ km, where this wave has a low intrinsic frequency.

4 Summary and Discussion

The close approach of a superpressure balloon and 6-day dwell time to a nearby radiosonde site in the near-equatorial Western Pacific allows a detailed study of grav-

ity waves by providing complementary information on vertical wave structure. The SPB provides high time resolution measurement in an intrinsic reference frame as function of time and space, but only at a fixed altitude. The radiosonde measurements provide twice-daily snapshots of the wave field as a function of height, but only at a single location. Sonde-derived wind and temperature fields also provide context for wave propagation in the vertical. At the time of the SPB passage near Momote the zonal winds at the 19.4 km float altitude transitioned from the eastward to the westward phase of the QBO.

We focus here on two large amplitude GW packets that have intrinsic periods near 1 day and 3 days, respectively. Wave properties derived from an S-transform analysis of the SPB data are supported by a Stokes analysis of the radiosonde observations. Both waves have short vertical wavelengths of a few km in the lower stratosphere but both have large horizontal scales, which in the case of the near 3-day wave is estimated to be over five thousand km. Vertical propagation of the shorter period, westward propagating, wave, is inhibited by a critical level at 20 km, but the longer period, eastward propagating, wave is able to travel into the middle stratosphere. These case studies allow us to estimate the impact of single wave events on wave driving of the QBO and on tropical cold-point temperatures (CPT).

An important attribute of the SPB observations is that they can provide estimates of the GW momentum flux for each packet (Table 2) and hence, via equation (2) allow the drag forces to be estimated if the height region over which each of the waves are dissipated is known. However, (2) by itself is inadequate to assess the impact of the waves on the QBO; one must also consider the duration and the scale of the forcing compared to the zonal mean. For these long period wave events, we can assume they are acting on a time scale of at least ∼1 day, and in the case of packet 2 several days and because for these are large scale waves the force is distributed over very large horizontal regions. Accordingly, an additional parameter, the area factor, A_{fac}, is required. This is simply defined as the area of wave packet dissipation normalized by the area of the zonal mean, which in turn can be simplified to be the zonal length of the wave packet dissipation area divided by the circumference of the earth. Assuming that the packet size is approximately 2-3 times the horizontal wavelength, λ_h, then $A_{fac} \sim 2 - 3 \times \lambda_h/40000$. Hence the zonal mean force is

$$\overline{F}_{zonal} = \overline{F}_{local} \times A_{fac} \tag{14}$$

–19–

412 where F_{local} is given by Eqn. (2).

413 For packet 1, the momentum flux = 4.6 mPa at the SPB float altitude and the wave

414 has a $\lambda_h = 970$ km. Assuming the dissipation occurs over $\Delta z \sim 600$ m and $\rho_o = 0.1$

415 kg m^{-3} then $\overline{F}_{local} \sim -6.6$ ms^{-1}day^{-1} while $A_{fac} \sim 2-3\times(970/40000)$, so the zonal

416 mean force is $\overline{F}_{zonal} \sim 0.3 - 0.5$ ms^{-1}day^{-1} and acts for about one day.

417 Based on time series of the QBO in April-May 2010, packet 2 would encounter its

418 own critical level at a height near 30 km or 10 hPa, where the density is $\rho_o = 0.022$ kg

419 m^{-3}. If the eastward flux is dissipated over a height range of $\Delta z \sim 2$ km then $\overline{F}_{local} \sim$

420 1.5 ms^{-1}day^{-1}. In this case the area factor is $A_{fac} \sim 2 - 3 \times (5350/40000) \sim 0.27 -$

421 0.40, so the zonal mean force is estimated to be $\overline{F}_{zonal} \sim 0.4 - 0.6$ ms^{-1}day^{-1} and it

422 will act for several days. Despite the smaller peak flux, packet 2 has a bigger impact than

423 packet 1 because it dissipates at a higher altitude, where the density is lower, and its large

424 scale and long duration means that its forcing is exerted over longer temporal and spa-

425 tial scales.

426 To place these results in context, we note that Jewtoukoff et al. (2013) derived the

427 average momentum fluxes for waves with periods shorter than a day for SPB flights 1

428 and 2 in the tropics. They reported average fluxes of about 5 mPa, but found the fluxes

429 to be highly intermittent; peak values of several hundreds mPa could be reached on timescales

430 of an hour or so. These high events were mostly tied to both convective sources. In terms

431 of individual packets, a similar large-scale gravity wave was observed using a cluster of

432 radiosonde observations near Darwin Australia (Evan & Alexander, 2008). Their case

433 study found a wave with a 2-day period and horizontal wavelength of $\sim$7000km prop-

434 agating southeastward, but the analysis suggested much smaller momentum fluxes than

435 we observe here.

436 The total zonal-mean force needed to drive the QBO is roughly 0.3-1.0 ms^{-1}day^{-1}

437 depending on altitude and phase of the QBO, and contributions from Kelvin waves roughly

438 half of that during the westerly phase of the QBO (M. J. Alexander & Ortland, 2010).

439 The wave events we observe here near Momote are contributing a substantial fraction

440 (50-100%) of the total wave force needed to drive the QBO, albeit for only for a few short

441 days of time. If one assumes similar waves occur fairly continuously at other locations

442 and times, then we could easily account for the necessary gravity wave driving of the QBO

443 with gravity waves of this type. Of particular note, is the fact that the 1-day wave im-

parts a significantly strong force near 20 km in the lower stratosphere. Gravity wave parameterizations tend to give much weaker forces at these low levels, and instead tend to contribute primarily to the upper levels of the QBO. In fact this tendency for parameterized gravity wave drag to be weak in the lower stratosphere may be why most models simulate weaker than observed QBO amplitudes in the lower stratosphere (Bushell et al., 2020).

Observations show that short vertical scale waves also cause temperature variations near the tropical tropopause with impacts on cold point temperatures (CPT), cirrus cloud occurrence, changes in stratospheric water vapor, turbulent layers, and vertical mixing (Kim & Alexander, 2015; Kim et al., 2016; Jensen et al., 2017; Podglajen et al., 2017). In particular, radiosondes launched from tropical sites in the Western Pacific indicate that collectively, tropical waves reduce the average CPT by 1.6 K relative to seasonal means, leading to stratospheric water vapor concentrations ∼25% lower than would occur in the absence of tropical waves (Kim & Alexander, 2015), and with associated surface temperature impacts (Solomon et al., 2010). Radiosonde profiles from Momote suggest that the two wave events in this study lowered the CPT by 2-3 K below the 7-day running mean temperature.

At the time of submission of this manuscript, a new set of tropical superpressure balloon measurements are currently being made and analyzed as part of the Strateole-2 test campaign, with balloon launches in late November to early December 2019. Haase et al. (2018) describe the plans for this campaign, which includes measurements from several high-resolution vertical profiling instruments. These data have yet to be fully analyzed, but our study provides an example of the additional information on tropical waves that can be obtained by combining high-vertical resolution profile measurements with superpressure balloon *in situ* wind and pressure measurements..

References

Alexander, M. J., & Holt, L. A. (2019). The Quasi-Biennial Oscillation and its influences at the surface. *US Clivar Variations*, *17*(1), 20-26. doi: 10.5065/q3jb -9642

Alexander, M. J., & Ortland, D. A. (2010). Equatorial waves in High Resolution Dynamics Limb Sounder (HIRDLS) data. *J. Geophys. Res. Atmos.*, *115*(D24111). doi: 10.1029/2010JD014782

Alexander, S. P., Tsuda, T., Kawatani, Y., & Takahashi, M. (2008). Global distribution of atmospheric waves in the equatorial upper troposphere and lower stratosphere: COSMIC observations of wave mean flow interactions. *J. Geophys. Res.*, *113*(D24), D24115. doi: 10.1029/2008JD010039

Allen, S. J., & Vincent, R. A. (1995). Gravity wave activity in the lower atmosphere: Seasonal and latitudinal variations. *J. Geophys. Res*, *100*, 1327-1350.

Boccara, G., Hertzog, A., Vincent, R. A., & Vial, F. (2008). Estimation of gravity-wave momentum fluxes and phase speeds from quasi-Lagrangian stratospheric balloon flights. 1: Theory and simulations. *J. Atmos. Sci.*, *65*, 3042–3055.

Boer, G. J., & Hamilton, K. (2008). QBO influence on extratropical predictive skill. *Climate Dynamics*, *31*(7), 987–1000. doi: 10.1007/s00382-008-0379-5

Bushell, A. C., Anstey, J. A., Butchart, N., Kawatani, Y., Osprey, S. M., Richter, J. H., . . . Yukimoto, S. (2020). Evaluation of the Quasi-Biennial Oscillation in global climate models for the SPARC QBO-initiative. *Q. J. R. Meteorol. Soc.*, (in press). doi: 10.1002/qj.3765

Butchart, N., Anstey, J. A., Hamilton, K., Osprey, S., McLandress, C., Bushell, A. C., . . . Yukimoto, S. (2018). Overview of experiment design and comparison of models participating in phase 1 of the SPARC Quasi-Biennial Oscillation initiative (QBOi). *Geoscientific Model Development*, *11*(3), 1009-1032. doi: 10.5194/gmd-11-1009-2018

Eckermann, S. D. (1996). Hodographic analysis of gravity waves: Relationships among stokes parameters, rotary spectra and cross-spectral methods. *J. Geo-*

508 *phys. Res.-Atmospheres*, *101*, 19169–19174. doi: 10.1029/96JD01578

509 Eckermann, S. D., & Vincent, R. A.   (1989).   Falling sphere observations of

510   anisotropic gravity wave motions in the upper stratosphere over Australia.

511   *Pure Applied Geophys.*, *130*, 510–532.

512 Evan, S., & Alexander, M. J.   (2008).   Intermediate-scale tropical inertia grav-

513   ity waves observed during the TWP-ICE campaign.   *J. Geophys. Res.-*

514   *Atmospheres*, *113*. doi: 10.1029/2007JD009289

515 Fritts, D. C., & Alexander, M. J.   (2003).   Gravity wave dynamics and effects in the

516   middle atmosphere. *Rev. Geophys.*, *41*, 1003, doi:10.1029/2001RG000106.

517 Gardner, C. S., & Gardner, N. F.   (1993).   Measurement distortion in aircraft, space

518   shuttle, and balloon observations of atmospheric density and temperature per-

519   turbation spectra. *J. Geophys. Res.*, *98*, 1023–1033. doi: 10.1029/92JD02025

520 Garfinkel, C., I, Schwartz, C., Domeisen, D. I., V, Son, S.-W., Butler, A. H., &

521   White, I. P.   (2018).   Extratropical atmospheric predictability from the

522   Quasi-Biennial Oscillation in subseasonal forecast models.   *J. Geophys. Res.-*

523   *Atmospheres*, *123*(15), 7855-7866. doi: 10.1029/2018JD028724

524 Geller, M. A., & Gong, J.   (2010).   Gravity wave kinetic, potential, and vertical fluc-

525   tuation energies as indicators of different frequency gravity waves.   *J. Geophys.*

526   *Res. Atmos.*, *115*, D11111. doi: 10.1029/2009JD012266

527 Giorgetta, M. A., Manzini, E., & Roeckner, E.   (2002).   Forcing of the quasi-biennial

528   oscillation from a broad spectrum of atmospheric waves.   *Geophys. Res. Lett.*,

529   *29*(8), 86-1–86-4. doi: 10.1029/2002GL014756

530 Gong, J., & Geller, M. A.   (2010).   Vertical fluctuation energy in United States high

531   vertical resolution radiosonde data as an indicator of convective gravity wave

532   sources. *J. Geophys. Res. Atmos.*, *115*, D11110. doi: 10.1029/2009JD012265

533 Haase, J. S., Alexander, M. J., Hertzog, A., Kalnajs, L., Deshler, T., Davis,

534   S. M., . . . Venel, S.   (2018).   Around the world in 84 days.   *Eos*, *99*.   doi:

535   10.1029/2018EO091907

536 Hertzog, A., Alexander, M. J., & Plougonven, R.   (2012).   On the intermittency of

537   gravity wave momentum flux in the stratosphere. *J. Atmos. Sci.*, *69*(11), 3433-

538   3448. doi: 10.1175/JAS-D-12-09.1

539 Hertzog, A., Boccara, G., Vincent, R. A., Vial, F., & Cocquerez, P.   (2008).   Estima-

540   tion of gravity-wave momentum fluxes and phase speeds from quasi-lagrangian

541 stratospheric balloon flights. 2: Results from the Vorcore campaign in Antarc-

542 tica. *J. Atmos. Sci.*, *65*, 3056–3070. doi: 10.1175/2008JAS2710.1

543 Hertzog, A., Vial, F., Mechoso, C. R., Basdevant, C., & Cocquerez, P.   (2002).

544 Quasi-Lagrangian measurements in the lower stratosphere reveal an energy

545 peak associated with near-inertial waves.   *Geophys. Res. Lett,*, *29*(8), 701–704.

546 doi: 10.1029/2001GL014083

547 Holt, L. A., Alexander, M. J., Coy, L., Molod, A., Putman, W., & Pawson, S.

548 (2016).   Tropical waves and the quasi-biennial oscillation in a 7-km global

549 climate simulation. *J. Atmos. Sci.*, *73*. doi: 10.1175/JAS-D-15-0350.1

550 Jensen, E. J., Pfister, L., Jordan, D. E., Bui, T. V., Ueyama, R., Singh, H. B., . . .

551 Pfeilsticker, K.   (2017).   The NASA Airborne Tropical Tropopause Ex-

552 periment: High-altitude aircraft measurements in the tropical Western Pa-

553 cific.   *Bulletin of the American Meteorological Society*, *98*, 129-143.   doi:

554 10.1175/BAMS-D-14-00263.1

555 Jewtoukoff, V., Plougonven, R., & Hertzog, A.   (2013).   Gravity waves generated by

556 deep tropical convection: estimates from balloon observations and mesoscale

557 simulations. *J. Geophys. Res.*, *118*, 9690–9707. doi: 10.1002/jgrd.50781

558 Kawatani, Y., & Hamilton, K. (2013). Weakened stratospheric quasibiennial oscilla-

559 tion driven by increased tropical mean upwelling.   *Nature*, *497*(7450), 478–481.

560 doi: 10.1038/nature12140

561 Kim, J.-E., & Alexander, M. J.   (2015).   Direct impacts of waves on tropical cold

562 point tropopause temperature. *Geophys. Res. Lett.*, *42*(5), 1584-1592. doi: 10

563 .1002/2014GL062737

564 Kim, J.-E., Alexander, M. J., Bui, T. P., Dean-Day, J. M., Lawson, R. P., Woods,

565 S., . . . Jensen, E. J.   (2016).   Ubiquitous influence of waves on trop-

566 ical high cirrus clouds.   *Geophys. Res. Lett.*, *43*(11), 5895-5901.   doi:

567 10.1002/2016GL069293

568 Lane, T. P., Reeder, M. J., & Guest, F. M.   (2003).   Convectively generated gravity

569 waves observed from radiosonde data taken during MCTEX.   *Q. J. R. Meteo-*

570 *rol. Soc.*, *129*, 1731–1740. doi: 10.1256/qj.02.196

571 Lim, Y., Son, S.-W., Marshall, A. G., Hendon, H. H., & Seo, K.-H.   (2019).   In-

572 fluence of the QBO on MJO prediction skill in the subseasonal-to-seasonal

573 prediction models.   *Climate Dynamics*, *53*(3-4), 1681-1695.   doi: 10.1007/

s00382-019-04719-y

Long, C. (2015). *Radiosonde measurements from station Momote (2010-01)*. PAN-GAEA. Retrieved from `https://doi.org/10.1594/PANGAEA.841567` doi: 10 .1594/PANGAEA.841474

Marks, C. J., & Eckermann, S. D. (1995). A three-dimensional nonhydrostatic ray-tracing model for gravity waves: Formulation and preliminary results for the middle atmosphere. *J. Atmos. Sci.*, *52*, 1959–1984.

Marshall, A. G., Hendon, H. H., & Son, S.-W. (2017). Impact of the quasi-biennial oscillation on predictability of the Madden–Julian oscillation. *Clim. Dyn.*, *49*(4), 1365—1377. doi: https://doi.org/10.1007/s00382-016-3392-0

Murphy, D. J., Alexander, S. P., Klekociuk, A. R., Love, P. T., & Vincent, R. A. (2014). Radiosonde observations of gravity waves in the lower stratosphere over Davis, Antarctica. *J. Geophys. Res. Atmos.*, *119*, 11,973–11,996. doi: 10.1002/2014JD022448

Nastrom, G. D. (1980). The response of superpressure balloons to gravity waves. *J. Applied Meteor.*, *19*, 1013–1019.

Podglajen, A., Bui, T. P., Dean-Day, J. M., Pfister, L., Jensen, E. J., Alexander, M. J., . . . Randel, W. J. (2017). Small-scale wind fluctuations in the tropical tropopause layer from aircraft measurements: Occurrence, nature, and impact on vertical mixing. *J. Atmos. Sci.*, *74*, 3847-3869. doi: 10.1175/JAS-D-17-0010.1

Podglajen, A., Hertzog, A., Plougonven, R., & Legras, B. (2016). Lagrangian temperature and vertical velocity fluctuations due to gravity waves in the lower stratosphere. *Geophys. Res. Lett,*, *43*(7), 3543–3553. doi: 10.1002/2016GL068148

Podglajen, A., Hertzog, A., Plougonven, R., & Žagar, N. (2014). Assessment of the accuracy of (re)analyses in the equatorial lower stratosphere. *J. Geophys. Res. Atmos.*, *119*, 11,166–11,188. doi: 10.1002/2014JD021849

Richter, J. H., Solomon, A., & Bacmeister, J. T. (2014). Effects of vertical resolution and nonorographic gravity wave drag on the simulated climate in the Community Atmosphere Model, version 5. *J. Adv. Modeling Earth Sys.*, *6*(2), 357–383. doi: 10.1002/2013MS000303

Scaife, A. A., Arribas, A., Blockley, E., Brookshaw, A., Clark, R. T., Dunstone,

607   N., . . . Williams, A.   (2014).   Skillful long-range prediction of European
608   and North American winters.   *Geophys. Res. Lett,*, *41*(7), 2514–2519.   doi:
609   10.1002/2014GL059637

610 Schöch, A., Baumgarten, G., Fritts, D. C., Hoffmann, P., Serafimovich, A., Wang,
611   L., . . . Schmidlin, F. J.   (2004).   Gravity waves in the troposphere and strato-
612   sphere during the MaCWAVE/MIDAS summer rocket program. *Geophys. Res.*
613   *Lett.*, *31*. doi: 10.1029/2004GL019837

614 Smith, D. M., Scaife, A. A., Eade, R., & Knight, J. R.   (2016).   Seasonal to
615   decadal prediction of the winter North Atlantic Oscillation: emerging capa-
616   bility and future prospects.   *Q. J. R. Meteorol. Soc.*, *142*(695), 611-617.   doi:
617   10.1002/qj.2479

618 Solomon, S. K., Rosenlof, K. H., Portman, R. W., Daniel, J. S., Davis, S. M., San-
619   ford, T. J., & Plattner, G. K.   (2010).   Contributions of stratospheric water
620   vapor to decadal changes in the rate of global warming.   *Science*, *327*, 1219–
621   1223. doi: 10.1126/science.1182488

622 Stockwell, R. G., Mansinha, L., & Lowe, R. P.   (1996).   Localization of the complex
623   spectrum: the S transform. *IEEE Transactions on Signal Processing*, *44*, 998–
624   1001. doi: 10.1109/78.492555

625 Tsuda, T., Murayama, Y., Wiryosumarto, H., Harijono, S. W. B., & Kato, S. (1994).
626   Radiosonde observations of equatorial atmosphere dynamics over Indonesia 2.
627   characteristics of gravity waves. *J. Geophys. Res.*, *99*, 10,507–10,516.

628 Vial, F., Hertzog, A., Mechoso, C. R., Badevent, C., Coquerez, P., Dubourg, V., &
629   Nouel, F.   (2001).   A study of the dynamics of the equatorial lower atmosphere
630   by use of ultra-long-duration balloons 1. Planetary scales.   *J. Geophys. Res.*
631   *Atmos.*, *106*, 22,725–22,743.

632 Vincent, R. A., & Alexander, M. J.   (2000).   Gravity waves in the tropical lower
633   stratosphere: An observational study of seasonal and interannual variability. *J.*
634   *Geophys. Res. Atmos.*, *105*, 17971–17982. doi: 10.1029/2000JD900196

635 Vincent, R. A., Allen, S. J., & Eckermann, S. D. (1997). Gravity-wave parameters in
636   the lower stratosphere.   In K. Hamilton (Ed.), *Gravity Wave Processes* (pp. 7–
637   25). Berlin, Heidelberg: Springer Berlin Heidelberg.

638 Vincent, R. A., & Fritts, D. C. (1987). A climatology of gravity wave motions in the
639   mesopause region at Adelaide, Australia.   *J. Atmos. Sci.*, *44*(4), 748–760.   doi:

640   10.1175/1520-0469(1987)044⟨0748:ACOGWM⟩2.0.CO;2

641 Vincent, R. A., & Hertzog, A. (2014). The response of superpressure balloons to

642   gravity wave motions. *Atmos. Meas. Tech.*, *7*, 1043–1055. doi: 10.5194/amt-7

643   -1043-2014

644 Vincent, R. A., Hertzog, A., Boccara, G., & Vial, F. (2007). Balloon-borne measure-

645   ments of gravity-wave momentum fluxes in the polar stratosphere. *Geophys.*

646   *Res. Lett.*, *34*, L19804. doi: 10.1029/2007GL031072

647 Wang, L., & Geller, M. A. (2003). Morphology of gravity-wave energy as observed

648   from 4 years (1998–2001) of high vertical resolution U.S. radiosonde data. *J.*

649   *Geophys. Res.*, *108*, 4489. doi: 10.1029/2002JD002786

650 Wang, L., Geller, M. A., & Alexander, M. J. (2005). Spatial and temporal vari-

651   ations of gravity wave parameters. part I: Intrinsic frequency, wavelength,

652   and vertical propagation direction. *J. Atmos. Sci.*, *62*, 125–142. doi:

653   10.1175/JAS-3364.1

654 Wright, C. J., Rivas, M. B., & Gille, J. C. (2011). Intercomparisons of HIRDLS,

655   COSMIC and SABER for the detection of stratospheric gravity waves. *Atmos.*

656   *Meas. Tech.*, *4*(8), 1581–1591. doi: 10.5194/amt-4-1581-2011